ACES Asian Chemical Editorial Society

doi.org/10.1002/asia.202500768

CHEMISTRY
AN ASIAN JOURNAL
Research Article

www.chemasianj.org

Interfacial Engineered Perylene Diimide Sensitized Photocathode for Enhanced Photoelectrocatalytic Energy-Demanding Reduction Reactions

Weijian Yang,[a] Pengju Li,[a] Zijian Zhao,[a] Limei Tian,[a] Fushuang Niu,[a, c] Renato N. Sampaio,*[d] and Ke Hu*[a, b]

Dye-sensitized photoelectrochemical cells (DSPECs) are emerging inexpensive devices for solar fuels production and chemical upgrading, yet their efficiency remains limited by poor photocurrent density especially in energy-demanding reactions. Here, we introduce a molecularly engineered photocathode that integrates perylene diimides (PDI)—capable of consecutive photoinduced electron transfer (ConPET) to generate an excited state (PDI^{2-*}) with potent reducing power—on a transparent conductive indium tin oxide nanoparticle (nanoITO) thin film substrate. By introducing an Al_2O_3 atomic layer via atomic layer deposition (ALD) onto the interface of PDI and nanoITO, the nonproductive back-electron transfer (BET) was significantly suppressed by over 95%, as quantified by transient absorption spectroscopy, while preserving the exceptional photoredox activity of PDI^{2-*}. This novel photocathode enables efficient activation of energy-demanding reduction reactions requiring highly negative reduction potentials, exemplified by the dehalogenation of 4-bromoacetophenone. This work demonstrates a novel approach for DSPECs, prioritizing interfacial control to unlock the potential of energy-demanding photoredox transformations.

1. Introduction

The direct conversion of solar energy into storable fuels is pivotal for addressing global energy challenges and achieving carbon neutrality.[1,2] Dye-sensitized photoelectrochemical cells (DSPECs) have emerged as versatile platforms for solar-driven synthesis of fuels and chemicals from abundant resources such as water[3–6] and CO_2.[7,8] While photoanodes based on wide-bandgap oxides (e.g., TiO_2, SnO_2) achieve a photocurrent densities in the mA cm^{-2} range,[9–11] the overall efficiency of tandem DSPECs remains bottlenecked by underperforming photocathodes.[12–14] State-of-the-art dye-sensitized photocathodes rely on p-type semiconductors such as NiO, yet suffer from low hole-mobility[15] and rapid charge recombination rates,[16,17] resulting in poor photoelectrochemical (PEC) performance and photocurrent densities commonly below 100 μA cm^{-2}.[16,18–20] A few photocathodes demand excessive material engineering for better performance.[21,22]

Dye-sensitized transparent conductive indium tin oxide nanoparticle (nanoITO) thin film electrodes are an inexpensive and easily prepared alternative to p-type metal oxides, the high conductivity and visible-light transparency render nanoITO an ideal substrate for investigating the electrochemical, photochemical, and photophysical properties of surface-bound molecular species and assemblies.[23–27]

Conventional dye-sensitized photocathodes operate through a well-established mechanism: photoexcited chromophores inject holes into p-type semiconductors (e.g., NiO), while their reduced states mediate substrate reduction.[16,28] However, this approach faces intrinsic limitations in driving energy-demanding reductions due to the limited redox potential of visible-light-absorbing chromophores.[29] This limitation has been circumvented through molecular photoredox innovations, where photocatalysts such as perylene diimides (PDI) enable potent reducing power via consecutive photoinduced electron transfer (ConPET).[30,31] Through sequential photon absorption, PDI generates a doubly reduced excited state (PDI^{2-*}) delivering reduction potentials more negetive than −2.4 V versus NHE—significantly surpassing conventional photosensitizers.[32,33] Integrating PDI^{2-*} with conductive nanoITO creates hybrid architectures capable of activating energy-demanding transformations. However, the high conductivity of nanoITO enables detrimental back-electron transfer (BET) from photoexcited PDI^{2-*}, diverting photogenerated electrons

[a] W. Yang, Dr. P. Li, Dr. Z. Zhao, L. Tian, Prof. F. Niu, Prof. K. Hu
Department of Chemistry and Shanghai Key Laboratory of Molecular Catalysis and Innovative Materials, Fudan University, 220 Handan Road, Shanghai 200433, P. R. China
E-mail: khu@tongji.edu.cn
khu@fudan.edu.cn

[b] Prof. K. Hu
School of Chemical Science and Engineering, Tongji University, 1239 Siping Road, Shanghai 200092, P. R. China

[c] Prof. F. Niu
School of Materials Science and Engineering, Linyi University, Linyi, Shandong 276000, P. R. China

[d] Prof. R. N. Sampaio
Department of Chemistry, University of North Carolina Chapel Hill, Chapel Hill, North Carolina 27599, USA
E-mail: renatons@email.unc.edu

Supporting information for this article is available on the WWW under https://doi.org/10.1002/asia.202500768

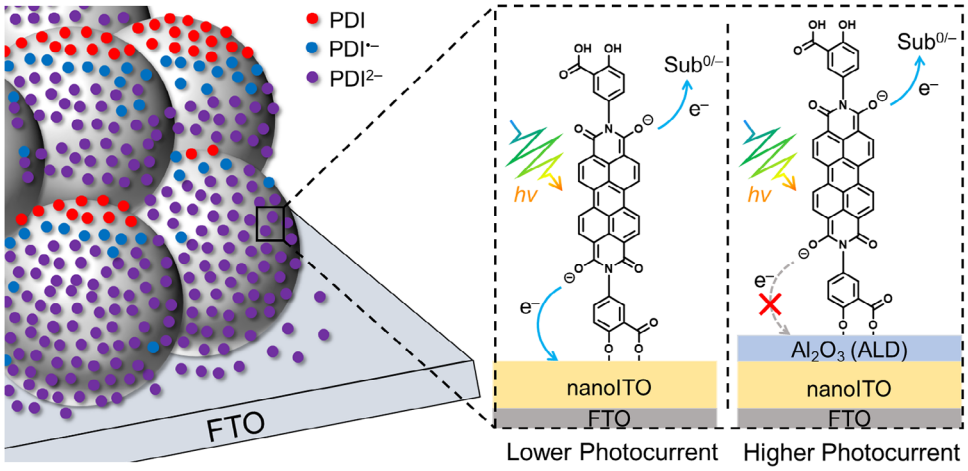

Figure 1. Schematic illustration of interfacial species evolution and photoinduced charge transfer processes in the ITO|Al_2O_3|PDI photocathode system.

from catalytic pathways.[34,35] To address this, we engineered an atomic-scale Al_2O_3 interlayer at the dye-semiconductor interface via atomic layer deposition (ALD), which can not only provide anchoring sites for molecular sensitizers,[36–38] but also significantly suppresses BET by modulating interfacial charge transfer dynamics.[39,40]

The resulting PDI sensitized Al_2O_3 atomic layer deposited nanoITO photocathode (hereafter abbreviated as ITO|Al_2O_3|PDI) achieves efficient photoelectrochemical dehalogenation of energy-demanding substrates such as 4-bromoacetophenone. Transient absorption (TA) spectroscopy validated that the Al_2O_3 interlayer effectively suppresses undesirable BET, reducing the yield of BET by 20-fold. This work establishes a molecular-level understanding for dye-sensitized photocathodes and paves the way for potential energy-demanding reduction reactions in DSPECs (Figure 1).

2 Results and Discussion

2.1 Fabrication and Characterization of Photocathodes

The ITO|Al_2O_3|PDI photocathode was fabricated through sequential nanofabrication processes. Presynthesized nanoITO colloids were deposited on FTO substrates via doctor-blade technique using sol-gel precursors, followed by thermal annealing at 450 °C for 2 h in air to form the nanoITO film.[26] Atomic layer deposition (ALD) with trimethylaluminum/water precursors at 150 °C precisely constructed an Al_2O_3 atomic layer on the nanoITO film,[41] followed by self-assembly of perylene diimide (PDI) molecules through carboxylate anchoring to the nanoporous electrode (Figure 2a). High-resolution transmission electron microscopy (HRTEM) analysis revealed well-defined stratified layers with lattice spacings of 0.36 nm (nanoITO (220)) and 0.26 nm (Al_2O_3 (104)), and the thickness of the Al_2O_3 layer can be observed to be about 4.0 nm (Figure 2b). UV–vis absorption spectroscopy analysis demonstrated that the composite electrode displayed optical absorption characteristics in the 400–600 nm range perfectly aligned with the distinctive absorption peaks of PDI molecules,[42] whereas the blank ITO|Al_2O_3 electrode exhibited negligible visible light absorption (Figure 2c).

Cyclic voltammetry demonstrated the reduction behavior of PDI molecules on the ITO|Al_2O_3 electrode interface, revealing two reversible redox peaks that correspond to the successive electrochemical reductions of $PDI^{0/\bullet-}$ (−0.34 V versus NHE) and $PDI^{\bullet-/2-}$ (−0.61 V versus NHE), respectively.[30] Spectroelectrochemical measurements captured the dynamic transformation of surface species from PDI to $PDI^{\bullet-}$ and ultimately to PDI^{2-} as the applied potential (E_{app}) scanned negatively from 0 to −1.0 V versus NHE. This evolution was characterized by a decrease in PDI absorption within 400–515 nm, accompanied by the emergence of $PDI^{\bullet-}$ radical anion signatures across 570–1000 nm, followed by their decay and the concurrent rise of PDI^{2-} absorption features spanning 515–700 nm (Figure 2d). Figure 2e shows the mole fractions of the PDI, $PDI^{\bullet-}$ and PDI^{2-} as a function of E_{app}. By fitting the species changes under different E_{app} using the Nernst equation, the redox potentials of $PDI^{0/\bullet-}$ and $PDI^{\bullet-/2-}$ can be calculated to be approximately −0.35 V versus NHE and -0.64 V versus NHE respectively,[43,44] which are approximately the same as those in the cyclic voltammetry tests. These observations provide experimental evidence that PDI^{2-} serves as a key photoactive species in the DSPEC process.

1.1. PEC Performance for Energy-Demanding Reduction Reactions

The PEC performance was systematically evaluated using 4-bromoacetophenone (E_{red} = −1.6 V versus NHE) as a redox-challenging substrate. Chopped light linear sweep voltammetry (LSV) revealed distinct photoresponsive characteristics of different photocathodes: pristine ITO and ITO|Al_2O_3 electrodes showed negligible photocurrent across the tested range, while both ITO|PDI and ITO|Al_2O_3|PDI photocathodes exhibited potential-dependent activation with onset potentials at −0.6 V versus NHE (Figure 3a). This threshold aligns with the reduction potential of PDI^{2-} identified in previous cyclic voltammetry

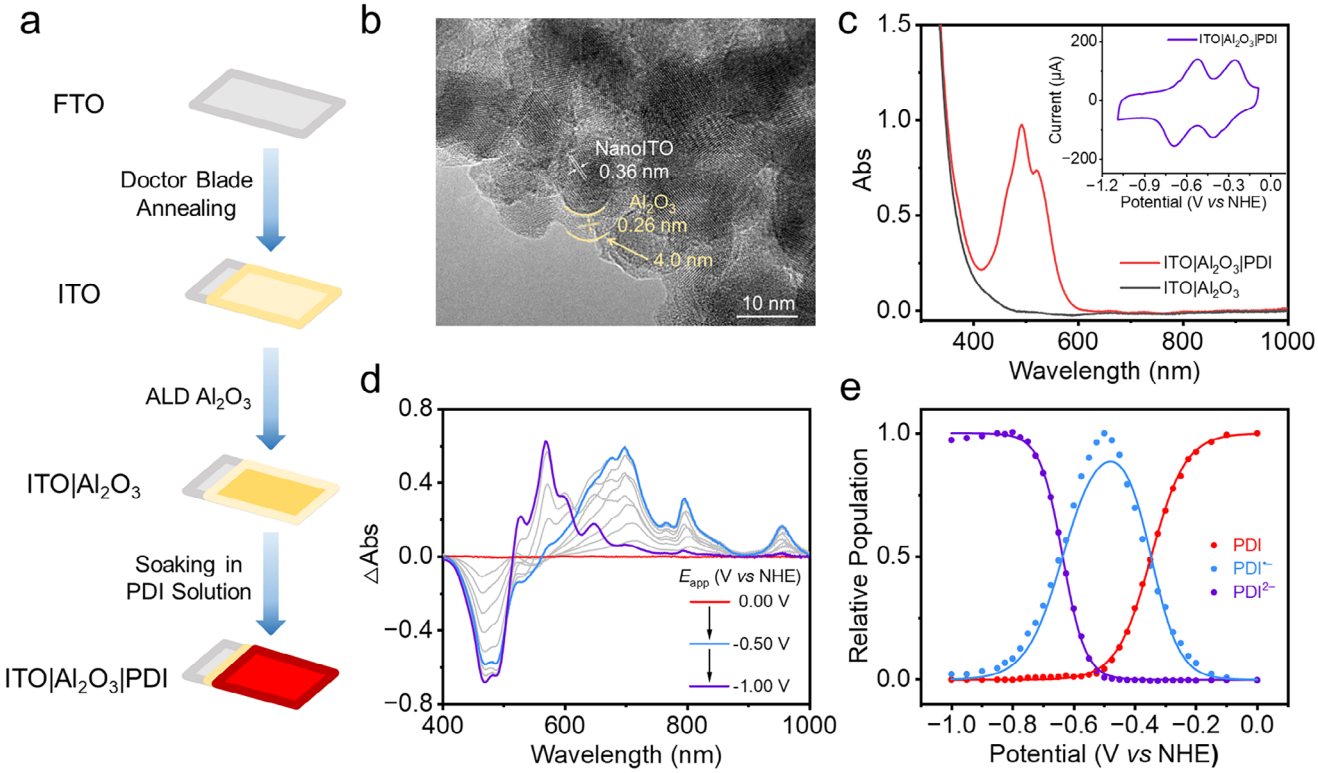

Figure 2. a) Schematic diagram of the fabrication of ITO|Al_2O_3|PDI photocathode. b) HRTEM images of ITO|Al_2O_3. c) UV–vis absorption spectra of ITO|Al_2O_3|PDI photocathode. Insert: Cyclic voltammogram of ITO|Al_2O_3|PDI photocathode. d) Spectroelectrochemistry of the ITO|Al_2O_3|PDI photocathode under varying E_{app}. e) Corresponding interfacial species change on the photocathode interface at different E_{app}. Overlaid is a fit to a modified Nernst equation (details see in the Supporting Information).

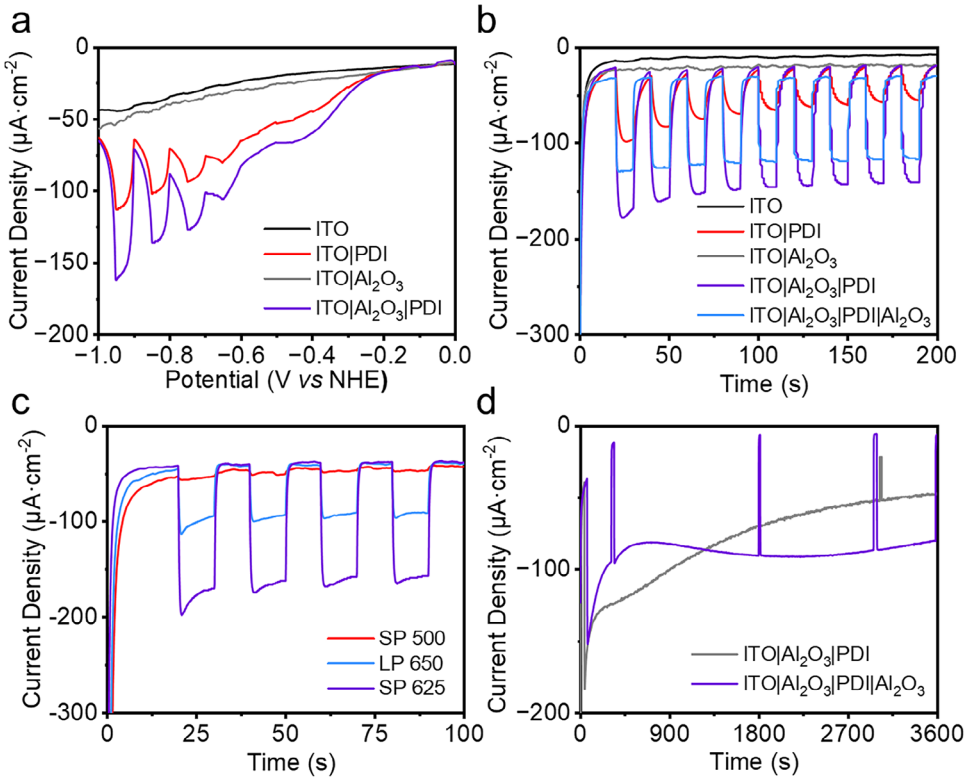

Figure 3. a) Chopped-light linear sweep voltammetry (LSV) curves of differently configured photocathodes. b) Photocurrent density-time (*J-t*) curves of differently configured photocathodes under chopped illumination. c) Wavelength-dependent chopped-light *J-t* curves of ITO|Al_2O_3|PDI photocathode. d) *J-* and *t* curves for 1 h long photostability tests of different photocathodes at −1.0 V versus NHE.

and spectroelectrochemical measurements, establishing a direct correlation between photocurrent generation and PDI^{2-} population dynamics. Control experiments with varying substrate concentrations demonstrated a significant increase in photocurrent density with increasing substrate concentration. Notably, no appreciable photocurrent generation was observed for the electrolyte (tetrabutylammonium perchlorate, TBAP), solvent (MeCN), and proton donors (isopropanol, IPA) in the absence of the substrate, directly confirming the photoelectrocatalytic reduction of the substrate at the photocathode surface (Figure S1).

As shown in Figure 3b, the chopped-light photocurrent density-time (*J–t*) curves of different photocathodes were measured under visible light illumination (100 mW cm^{-2}, White LED). *J-t* curves revealed significant photocurrent density and stability variations. The ITO|PDI photocathode exhibited rapid photocurrent density decay from 75 to 25 μA cm^{-2} over 200 s, whereas the ITO|Al_2O_3|PDI demonstrated significantly enhanced photocurrent density (155 μA cm^{-2},) with mitigated decay to 121 μA cm^{-2} under identical conditions, while delivering 2.1-fold higher photocurrent density. The thickness of Al_2O_3 atomic layer was systematically evaluated, revealing optimal photocurrent density (~155 μA cm^{-2}) at 4 nm thickness. Beyond this threshold, excessive Al_2O_3 deposition (>4 nm) induced substantial electron transport resistance due to the dielectric nature of Al_2O_3 which resulted in progressive photocurrent density decrease (Figure S2). In addition, we deposited an additional 1 nm Al_2O_3 protective overlayer on the ITO|Al_2O_3|PDI photocathode surface. While the insulating nature of the outer Al_2O_3 layer reduced the initial photocurrent density to 120 μA cm^{-2}, it effectively suppressed interfacial degradation, as evidenced by negligible photocurrent density decay over 200 s under continuous illumination.

The half-cell applied bias photon-to-current efficiency (HC-ABPE), serving as a straightforward metric for evaluating incident photon utilization in photoelectrochemical systems,[45,46] can be calculated by Equation (1).

$$\mathrm{HC-ABPE} = \frac{J_p \times \left(E^0 - E_{app}\right)}{P} \times 100\% \quad (1)$$

where J_p denotes the photocurrent density (mA cm^{-2}), E^0 represents the redox potential of the substrate (versus NHE), E_{app} represents the applied potential (versus NHE), and *P* corresponds to the incident light power density (100 mW cm^{-2}). The HC-ABPE profiles presented in Figure S3 were derived from chopped-light LSV measurements. Notably, the ITO|Al_2O_3|PDI photocathode modified with the Al_2O_3 interlayer demonstrated a twofold enhancement in HC-ABPE compared to the unmodified ITO|PDI counterpart, highlighting its superior efficiency in incident photon utilization. In addition, the intrinsic solar-to-chemical (ISTC) conversion efficiency demonstrated a 2-fold enhancement at an E_{app} of −1.0 V versus NHE for the ITO|Al_2O_3|PDI photocathode compared to ITO|PDI photocathode. This improvement confirms the pivotal role of the Al_2O_3 atomic layer in optimizing interfacial charge transfer dynamics, thereby significantly boosting the photon-to-chemical energy conversion efficiency.

The wavelength-dependent *J-t* curves revealed critical spectral characteristics of the system. Negligible photocurrent generation was generated under excitation wavelengths below 500 nm, while wavelengths exceeding 650 nm exhibited substantially reduced photocurrent density. Notably, illumination within the 500–625 nm range, fully encompassing the characteristic absorption band of PDI^{2-}, sustained a stable photocurrent density of ~150 μA cm^{-2}, consistent with white LED excitation performance (Figure 3c). This spectral alignment provides direct evidence for PDI^{2-} as the primary photoactive species.

Subsequently, we conducted a 1 h long photostability test shown in Figure 3d. The ITO|Al_2O_3|PDI photocathode exhibited rapid current density decay from an initial 180—50 μA cm^{-2}, with light-chopping analysis confirming a residual photocurrent density of ~30 μA cm^{-2} after 1 h. UV–vis spectroscopy revealed significant attenuation and spectral shifts in PDI absorption features before and after the PEC reaction, indicative of molecular degradation during prolonged photoelectrochemical operation (Figure S4). In contrast, the surface-engineered ITO|Al_2O_3|PDI|Al_2O_3 photocathode with an additional 1 nm Al_2O_3 overlayer demonstrated enhanced stability. Although displaying a lower initial photocurrent density (150 μA cm^{-2}, light-chopped value: 120 μA cm^{-2}), this configuration retained ~80 μA cm^{-2} after 1 h with minimal dark current interference. These results confirm the protective role of the outer Al_2O_3 layer in suppressing photocorrosion for sustained catalytic activity.

The optimized ITO|Al_2O_3|PDI|Al_2O_3 photocathode, exhibiting enhanced photocurrent density and operational stability in prior PEC performance evaluations, was subsequently employed for prolonged substrate conversion tests. Under an E_{app} of -1.0 V versus NHE with 4-bromoacetophenone as the substrate and IPA as the proton donor, the system achieved a faradaic efficiency (FE) of 74% after 4 h (Figures S5 and S6). The limited photocurrent density of the photocathode (~150 μA cm^{-2}) necessitates prolonged operational times for complete substrate conversion, simultaneously posing significant stability challenges to the electrode architecture. Consequently, this study focuses on reporting the FE, while achieving high-yield PEC systems requires further optimization in subsequent investigations, particularly through enhanced interfacial charge transfer kinetics and mitigation of long-term performance degradation mechanisms.

Critical control experiments established three fundamental requirements: 1) Strict photoelectrochemical synergy, as neither product formation nor current generation occurred under dark conditions or without E_{app}; 2) essential involvement of PDI^{2-} intermediates as the primary photoactive species, evidenced by complete catalytic inactivity at −0.5 V versus NHE where only $PDI^{\bullet-}$ species form; 3) vital interfacial engineering, as the unmodified ITO|PDI electrode exhibited drastically reduced FE (37%), underscoring the critical role of the Al_2O_3 interlayer in increasing PEC performance and ISTC (Table 1).

However, two other photosensitizer derivatized photoelectrodes (ITO|Al_2O_3|PBI and ITO|Al_2O_3|PDI-1, Figure S7a,b) showed negligible catalytic activity, likely due to insufficient excited-state reduction potentials or inadequate excited-state lifetimes of the photosensitizers for substrate activation (Figure S7c).

The iodo and chloro analogues of 4-bromoacetophenone were also used as dehalogenation substrates to evaluate the photocathode's generality. 4-iodoacetophenone with

Table 1. PEC dehalogenation reaction.[a]

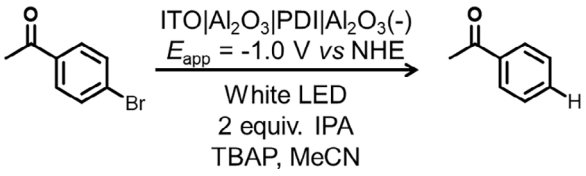

Entry	Deviation	FE (%)[b]
1	None	74%
2	No E_{app}	n.d.
3	No Light	n.d.
4	E_{app} = -0.5 V	n.d.
5	No Al_2O_3 layer	37%
6	PBI	n.d.
7	PDI-1	n.d.

[a] Reaction conditions: 0.1 M TBAP, 20 mM 4-bromoacetophenone, 40 mM isopropanol (IPA), 5 mL MeCN, white LED (100 mW cm^{-2}), 1 atm Ar. [b] FE was calculated by HPLC.

a lower reduction potential (−1.6 V versus NHE) and 4-chloroacetophenone with a higher reduction potential (-1.8 V versus NHE) demonstrated substantial photocurrent densities under identical operational conditions (Figure S8a,b). This systematic response across substrates with varying reduction potentials highlights the ITO|Al_2O_3|PDI photocathode's versatility in PEC activation of energy-demanding reductive transformations.

1.2. Mechanistic Investigation

The mechanistic insights into the PEC performance enhancement of the Al_2O_3 atomic layer in the photocathode were systematically investigated through nanosecond transient absorption (TA) spectroscopy. Under an E_{app} of −1.0 V versus NHE, the ITO|Al_2O_3|PDI photocathode undergoes reduction to form ITO|Al_2O_3|PDI^{2-}, where 580 nm pulsed laser generates the PDI^{2-*} excited state. The excited state electron transfer occurs from PDI^{2-*} to the substrate, generating photocurrent as illustrated in Equations 2 and 3.

$$ITO\left|Al_2O_3\right|PDI^{2-} \xrightarrow{h\nu} ITO\left|Al_2O_3\right|PDI^{2-*} \quad (2)$$

$$ITO\left|Al_2O_3|PDI^{2-*} + Sub \rightarrow ITO\right|Al_2O_3|PDI^{\bullet-} + Sub^{-} \quad (3)$$

Following photoexcitation and electron transfer, the PDI^{2-} species converts to $PDI^{\bullet-}$, which subsequently regenerates to PDI^{2-} via electrochemical reduction, completing the catalytic cycle. Crucially, the excited-state electron transfer exhibit dual pathways: besides substrate reduction, an undesirable back-electron transfer (BET) to the ITO electrode could occur, resulting in decreased photocurrent (Equation 4).

$$ITO\left|Al_2O_3|PDI^{2-*} \rightarrow ITO\left(e^{-}\right)\right|Al_2O_3|PDI^{\bullet-} \quad (4)$$

Both two charge transfer routes induce PDI^{2-} depletion and $PDI^{\bullet-}$ formation, exhibiting indistinguishable spectral signatures in TA measurements. To isolate the back electron transfer pathway, TA measurements were conducted in 0.1 M TBAP acetonitrile solution without the substrate. The TA spectra of ITO|PDI^{2-} prominent $PDI^{\bullet-}$ characteristic signals and PDI^{2-} bleaching signals at microsecond time delays (Figure 4a). In the absence of substrates, these observations unequivocally originate from BET of PDI^{2-*} electron injection into the nanoITO, resulting in $PDI^{\bullet-}$ formation and PDI^{2-} depletion. This nonradiative electron transfer pathway competes with substrate reduction, thereby substantially diminishing photocurrent values and photon-to-current conversion efficiency. Notably, the introduction of an Al_2O_3 interlayer dramatically suppressed back-electron injection, as evidenced by the negligible signal of $PDI^{\bullet-}$ generation in TA spectra in the same time delays (Figure 4b).

Analysis of the initial amplitudes of the single-wavelength kinetic data at 700 nm, where $PDI^{\bullet-}$ absorbs significantly, revealed a 95% quantum yield suppression of BET in the ITO|Al_2O_3|PDI photocathode compared to the ITO|PDI photocathode (Figure 4c). Besides, the ITO|Al_2O_3|PDI photocathode exhibited enhanced sub-20 ns fluorescence intensity compared to ITO|PDI photocathode. This amplification arises from the Al_2O_3 interlayer suppressing BET of excited-state electrons to the nanoITO substrate—a dominant pathway for fluorescence quenching in DSPECs. This suppression again confirms the efficacy of Al_2O_3 atomic layer in blocking BET, thereby channeling photogenerated electrons toward interfacial catalytic reactions. Consequently, significant enhancements in photocurrent density and energy conversion efficiency were achieved.

2. Conclusion

In conclusion, this study presents a rationally designed ITO|Al_2O_3|PDI photocathode that demonstrates energy-demanding reductive dehalogenation of 4-bromoacetophenone. By integrating ALD of ultrathin Al_2O_3 interlayers with PDI sensitization, we achieved a 2,3-fold enhancement in photocurrent density (up to 155 μA cm^{-2}) compared to unmodified counterparts, with a faradaic efficiency of 74%. Transient absorption spectroscopy revealed that the 4 nm Al_2O_3 layer reduced BET efficiently and directing photogenerated electrons toward catalytic substrate reduction. Wavelength-selective experiments further confirmed PDI^{2-} as the photoactive species, with spectral alignment in the 500–625 nm range. Surface engineering with an additional 1 nm Al_2O_3 overlayer improved operational stability, albeit with reduced initial photocurrent density.

This work establishes a molecular-level strategy for engineering dye-semiconductor interfaces, offering a scalable pathway to nonprecious-metal photoelectrodes for energy-demanding reduction reactions. Future efforts should focus on mitigating long-term degradation through advanced passivation strategies while expanding the substrate scope to more challenging reductive transformations. The insights gained here underscore the

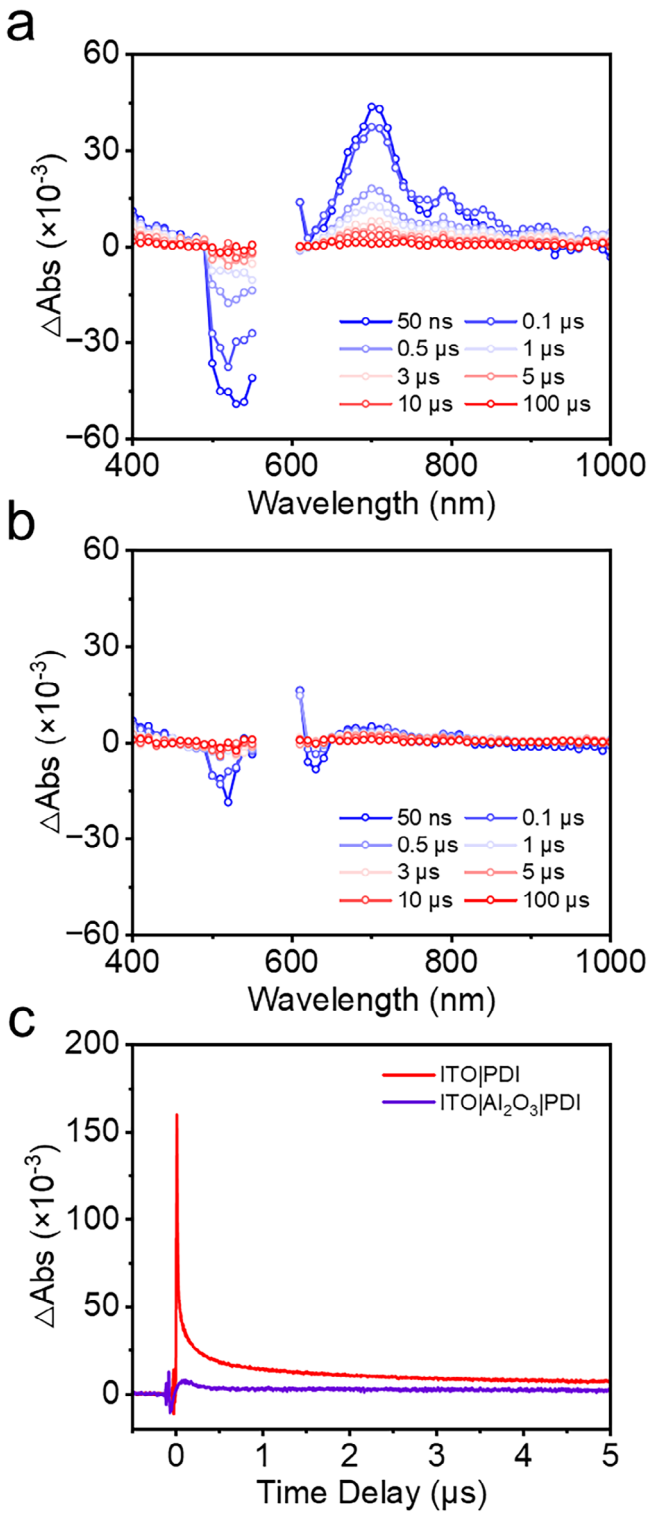

Figure 4. Transient absorption spectra measured after pulsed 580 nm laser excitation of a) ITO|PDI^{2-} and b) ITO|Al_2O_3|PDI^{2-} in 0.1 M TBAP MeCN solution without the substrate. c) Transient absorption kinetic traces monitored at 700 nm of $PDI^{\bullet-}$ formation using ITO|PDI^{2-} and ITO|Al_2O_3|PDI^{2-} photocathode in 0.1 M TBAP MeCN solution without the substrate.

potential of ALD-derived interfacial engineering in advancing artificial photosynthetic systems toward PEC synthetic applications.

Acknowledgments

This study is sponsored by National Key R&D Program of China (2023YFE0124100), National Natural Science Foundation of China (22173022), and the Fundamental Research Funds for the Central Universities.

Conflict of Interests

The authors declare no conflict of interest.

Data Availability Statement

The data that support the findings of this study are available from the corresponding author upon reasonable request.

Keywords: Atomic layer deposition · Back-electron transfer · Dye-sensitized photocathode · Interfacial engineering · Photoelectrochemical cells

[1] K. E. Dalle, J. Warnan, J. J. Leung, B. Reuillard, I. S. Karmel, E. Reisner, *Chem. Rev.* **2019**, *119*, 2752–2875.
[2] M. C. Lamb, K. A. Steiniger, L. K. Trigoura, J. Wu, G. Kundu, H. Huang, T. H. Lambert, *Chem. Rev.* **2024**, *124*, 12264–12304.
[3] M. V. Sheridan, Y. Wang, D. Wang, L. Troian-Gautier, C. J. Dares, B. D. Sherman, T. J. Meyer, *Angew. Chem. Int. Ed.* **2018**, *57*, 3449–3453.
[4] J. Z. Zhang, E. Reisner, *Nat. Rev. Chem.* **2020**, *4*, 6–21.
[5] P. Xu, N. S. McCool, T. E. Mallouk, *Nano Today* **2017**, *14*, 42–58.
[6] M. Grätzel, *Nature* **2001**, *414*, 338–344.
[7] F. Kuttassery, Y. Ohsaki, A. Thomas, R. Kamata, Y. Ebato, H. Kumagai, R. Nakazato, A. Sebastian, S. Mathew, H. Tachibana, O. Ishitani, H. Inoue, *Angew. Chem. Int. Ed.* **2023**, *62*, e202308956.
[8] D. N. Nguyen, E. Giannoudis, T. Straistari, J. Fize, M. Koepf, P. D. Tran, M. Chavarot-Kerlidou, V. Artero, *ACS Energy Lett.* **2024**, *9*, 829–834.
[9] L. Zhang, Y. Gao, X. Ding, Z. Yu, L. Sun, *ChemSusChem* **2014**, *7*, 2801–2804.
[10] Y. Zhu, X. Li, Z. Wen, R. Zhao, Z. Chen, Z. Zhang, H. Gao, S. Wang, F. Li, *J. Am. Chem. Soc.* **2024**, *146*, 21903–21912.
[11] G. M. Lana, I. T. Bello, O. M. Adedokun, V. O. Adenigba, P. R. Jubu, O. Adedokun, Y. K. Sanusi, M. S. Dhlamini, A. O. Awodugba, *Sol. Energy* **2024**, *279*, 112850.
[12] L. Fei, L. Lei, T. J. Meyer, D. Wang, *Acc. Mater. Res.* **2024**, *5*, 124–135.
[13] F. Li, K. Fan, B. Xu, E. Gabrielsson, Q. Daniel, L. Li, L. Sun, *J. Am. Chem. Soc.* **2015**, *137*, 9153–9159.
[14] F. Odobel, Y. Pellegrin, E. A. Gibson, A. Hagfeldt, A. L. Smeigh, L. Hammarström, *Coord. Chem. Rev.* **2012**, *256*, 2414–2423.
[15] R. J. Dillon, L. Alibabaei, T. J. Meyer, J. M. Papanikolas, *ACS Appl. Mater. Interfaces* **2017**, *9*, 26786–26796.
[16] V. Nikolaou, A. Charisiadis, G. Charalambidis, A. G. Coutsolelos, F. Odobel, *J. Mater. Chem. A* **2017**, *5*, 21077–21113.
[17] S. Zhang, H. Ye, H. Ding, F. Yu, J. Hua, *Sci. China Chem.* **2020**, *63*, 228–236.
[18] B. Shan, B. D. Sherman, C. M. Klug, A. Nayak, S. L. Marquard, Q. Liu, R. M. Bullock, T. J. Meyer, *J. Phys. Chem. Lett.* **2017**, *8*, 4374–4379.
[19] A. Bachmeier, S. Hall, S. W. Ragsdale, F. A. Armstrong, *J. Am. Chem. Soc.* **2014**, *136*, 13518–13521.
[20] J. Huang, J. Sun, Y. Wu, C. Turro, *J. Am. Chem. Soc.* **2021**, *143*, 1610–1617.
[21] J. Sun, Y. Wu, *Angew. Chem. Int. Ed.* **2020**, *59*, 10904–10908.

[22] K. A. Click, D. R. Beauchamp, Z. Huang, W. Chen, Y. Wu, *J. Am. Chem. Soc.* **2016**, *138*, 1174–1179.
[23] P. G. Hoertz, Z. Chen, C. A. Kent, T. J. Meyer, *Inorg. Chem.* **2010**, *49*, 8179–8181.
[24] B. H. Farnum, A. Nakada, O. Ishitani, T. J. Meyer, *J. Phys. Chem. C* **2015**, *119*, 25180–25187.
[25] B. H. Farnum, Z. A. Morseth, M. K. Brennaman, J. M. Papanikolas, T. J. Meyer, *J. Am. Chem. Soc.* **2014**, *136*, 15869–15872.
[26] B. H. Farnum, K.-R. Wee, T. J. Meyer, *Nat. Chem.* **2016**, *8*, 845–852.
[27] R. N. Sampaio, L. Troian-Gautier, G. J. Meyer, *Angew. Chem. Int. Ed.* **2018**, *57*, 15390–15394.
[28] K. Zhu, G. Mul, A. Huijser, *Chem. Phys. Rev.* **2024**, *5*, 021305.
[29] S. Wu, J. Kaur, T. A. Karl, X. Tian, J. P. Barham, *Angew. Chem. Int. Ed.* **2022**, *61*, e202107811.
[30] I. Ghosh, T. Ghosh, J. I. Bardagi, B. König, *Science* **2014**, *346*, 725–728.
[31] Y. Xu, J. Zheng, J. O. Lindner, X. Wen, N. Jiang, Z. Hu, L. Liu, F. Huang, F. Würthner, Z. Xie, *Angew. Chem. Int. Ed.* **2020**, *59*, 10363–10367.
[32] H. Li, O. S. Wenger, *Angew. Chem. Int. Ed.* **2022**, *61*, e202110491.
[33] M. Cybularczyk-Cecotka, J. Szczepanik, M. Giedyk, *Nat. Catal.* **2020**, *3*, 872–886.
[34] K. Tvrdy, P. A. Frantsuzov, P. V. Kamat, *Proc. Natl. Acad. Sci. USA* **2011**, *108*, 29–34.
[35] M. K. Brennaman, R. J. Dillon, L. Alibabaei, M. K. Gish, C. J. Dares, D. L. Ashford, R. L. House, G. J. Meyer, J. M. Papanikolas, T. J. Meyer, *J. Am. Chem. Soc.* **2016**, *138*, 13085–13102.
[36] H.-J. Son, C. H. Kim, D. W. Kim, N. C. Jeong, C. Prasittichai, L. Luo, J. Wu, O. K. Farha, M. R. Wasielewski, J. T. Hupp, *ACS Appl. Mater. Interfaces* **2015**, *7*, 5150–5159.
[37] W. Song, H. Wang, G. Liu, M. Peng, D. Zou, *Nano Energy* **2016**, *19*, 1–7.
[38] D. Wang, M. V. Sheridan, B. Shan, B. H. Farnum, S. L. Marquard, B. D. Sherman, M. S. Eberhart, A. Nayak, C. J. Dares, A. K. Das, R. M. Bullock, T. J. Meyer, *J. Am. Chem. Soc.* **2017**, *139*, 14518–14525.
[39] J. Song, A. Ge, B. Piercy, M. D. Losego, T. Lian, *Chem. Phys.* **2018**, *512*, 68–74.
[40] R. J. Kamire, K. L. Materna, W. L. Hoffeditz, B. T. Phelan, J. M. Thomsen, O. K. Farha, J. T. Hupp, G. W. Brudvig, M. R. Wasielewski, *J. Phys. Chem. C* **2017**, *121*, 3752–3764.
[41] J. S. Jur, G. N. Parsons, *ACS Appl. Mater. Interfaces* **2011**, *3*, 299–308.
[42] Z. Zhao, F. Niu, P. Li, H. Wang, Z. Zhang, G. J. Meyer, K. Hu, *J. Am. Chem. Soc.* **2022**, *144*, 7043–7047.
[43] E. J. Piechota, L. Troian-Gautier, R. N. Sampaio, M. K. Brennaman, K. Hu, C. P. Berlinguette, G. J. Meyer, *J. Am. Chem. Soc.* **2018**, *140*, 7176–7186.
[44] B. N. DiMarco, T. C. Motley, R. S. Balok, G. Li, M. A. Siegler, R. M. O'Donnell, K. Hu, G. J. Meyer, *J. Phys. Chem. C* **2016**, *120*, 14226–14235.
[45] B. Zhang, S. Yu, Y. Dai, X. Huang, L. Chou, G. Lu, G. Dong, Y. Bi, *Nat. Commun.* **2021**, *12*, 6969.
[46] S. Y. Chae, N. Yoon, E. D. Park, O. S. Joo, *Appl. Surf. Sci.* **2023**, *612*, 155856.

Manuscript received: June 8, 2025
Revised manuscript received: July 3, 2025
Version of record online: July 21, 2025